Journal of Computer Science and Artificial Intelligence
ISSN: 3078-8242 (Print), ISSN: 3078-2309 (Online) | Vol. 9, No. 2, 2026

Study of Hot-Air Drying of Chinese Medicinal Materials Using a Coupled Heat and Moisture Transfer Model

Yanan Chen, Xiaoyan Li, Mengyu Liu, Chen Fang, Yang Shen *

School of Mathematics and Big Data, Chaohu University, Chaohu, 238024, China

* **Corresponding author**: (Email: shenyang051127@gmail.com)

Abstract: Hot-air drying of Chinese medicinal materials involves coupled heat conduction, moisture diffusion, and shrinkage-induced changes in transport distance. This study formulates a one-dimensional axisymmetric model for a 25-cm-long cylindrical material with an initial radius of 2 cm, temperature of 28 °C, and dry-basis moisture content of 2.55 kg/kg. The model combines measured chamber conditions, state-dependent properties, conservative finite-volume discretization, fully implicit time stepping, and Picard iteration; measured shrinkage is mapped to a fixed computational interval. Under the fixed-radius model, the center reaches the 0.15 kg/kg drying threshold after 57.45 h, while the shrinkage-enabled configuration reaches it after 51.10 h. The volume-average criterion would declare the shrinking material dry at 34.38 h, 16.72 h before the center meets the threshold. Grid refinement and parameter perturbations support numerical stability, and the results show that endpoint evaluation must account for spatial moisture gradients and the prescribed shrinkage-dependent geometry and properties.

Keywords: Chinese Medicinal Materials, Hot-Air Drying, Coupled Heat and Moisture Transfer, Finite-Volume Method, Moving Boundary, Shrinkage.

1. Introduction

Hot-air drying is widely used to reduce moisture in herbal and food materials, but it is a coupled transport process rather than a simple mass-loss curve. Heat enters through the surface and conducts inward, while moisture diffuses outward; both rates depend on local temperature and moisture and may evolve as the material shrinks. Reviews of drying physics describe simultaneous heat, mass, and, in porous products, momentum transfer [1]. Numerical work has addressed conjugate heat and mass transfer with vaporization in a hot-air tunnel [2], while ginger models have resolved internal temperature and moisture gradients under staged air temperatures [3]. Porous-medium formulations have also been applied to heat-pump drying of sea cucumber [4]. Experiments on Chinese medicine residues further show long falling-rate periods dominated by internal moisture transport [5].

Shrinkage can alter diffusion paths and predicted drying rates. A convective jackfruit model explicitly compared shrinkage-enabled and fixed-geometry formulations [6], while studies of peppermint, basil, and lemon balm measured how convection and vacuum drying affect volatile and physicochemical properties [7]. Coupled heat and mass models have also been developed for jujube slices under hot-air and radio-frequency treatment [8]. Recent work extends these approaches to irregular materials with shrinkage-linked multiphysics and to geometry-aware shrimp drying models [9, 10]. Research on Chinese medicinal-material drying mechanisms and shrinkage factors likewise emphasizes botanical material-specific behavior [11, 12].

Despite this progress, drying a long cylindrical medicinal material raises a specific endpoint and geometry question. Moisture remains spatially nonuniform during falling-rate drying, so an average moisture value can mask a wet core; at the same time, contraction changes the diffusion distance and moves the external boundary. Reliable estimates matter because incomplete drying leaves wet regions, whereas unnecessary exposure can add energy use and degrade active constituents. This study models a 25-cm-long material with a 2-cm initial radius using a one-dimensional axisymmetric formulation. Measured chamber temperature and moisture histories define the time-varying surface conditions, and the measured radius trajectory defines the shrinking boundary. State-dependent thermal and moisture properties are incorporated into conservative finite-volume balances, advanced with a fully implicit scheme and Picard iteration. A material-coordinate transformation maps the moving domain to a fixed interval, allowing the associated equations to be solved on a stable radial grid. Drying completion is defined by the first time the maximum local dry-basis moisture content falls below 0.15 kg/kg. Grid convergence, simplified physical assumptions, and boundary-parameter sensitivity are also assessed. The study compares the fixed-radius and shrinkage-enabled calculations and interprets their difference in light of the different property correlations prescribed for the two configurations.

2. Model Formulation and Numerical Solution

2.1. Geometry, Measurements, And Assumptions

The material is represented as a 0.25-m-long cylinder with an initial radius of 0.02 m. Its initial temperature is 28 °C and its initial dry-basis moisture content is 2.55 kg/kg. Chamber temperature and moisture records contain 241 observations at 60-s intervals over 0–4 h; linear interpolation supplies values between observations. The measured radius history spans 0–72 h at 30-min intervals and is also interpolated. After 4 h, the chamber boundary is held at 50 °C and 0.05 kg/kg. The long-axis dimension is treated as uniform and end effects are omitted. Surface heat and moisture exchange are represented by convective boundary conditions with constant coefficients. Radiation, latent heat, internal vaporization and condensation, and shrinkage-induced internal convection are omitted,

consistent with the stated model assumptions.

Table 1 summarizes the baseline fixed-property values used for the preheating case. Full-cycle calculations replace constant properties with the empirical correlations specified for each modeled configuration.

Table 1. Geometry, initial state, and baseline fixed-property parameters.

Parameter	Value
Material length	0.25 m
Initial radius	0.020 m
Initial temperature	28 °C (301.15 K)
Initial dry-basis moisture	2.55 kg/kg
Density	820 kg/m³
Specific heat	2,600 J/(kg·K)
Thermal conductivity	0.36 W/(m·K)
Heat-transfer coefficient	25 W/(m²·K)
Mass-transfer coefficient	8×10^{-7} m/s

2.2. Coupled Transport Equations

For a fixed cylindrical domain, radial temperature and moisture fields follow conservation of energy and dry-matter-referenced moisture mass. Local material properties couple the two balances during full-cycle drying:

$$\rho c_p \frac{\partial T}{\partial t} = \frac{1}{r}\partial \frac{\partial}{\partial r}\left(rk \frac{\partial T}{\partial r}\right) \tag{1}$$

$$\frac{\partial C}{\partial t} = \frac{1}{r}\partial \frac{\partial}{\partial r}\left(rD \frac{\partial C}{\partial r}\right) \tag{2}$$

At the centerline, radial gradients vanish. At the surface, heat and moisture fluxes are balanced against chamber conditions through the measured convective coefficients:

$$\begin{aligned} \frac{\partial T}{\partial r}|_{\mathrm{r=0}} &= 0 \\ \frac{\partial C}{\partial r}|_{\mathrm{r=0}} &= 0 \end{aligned} \tag{3}$$

$$\begin{aligned} -k \frac{\partial T}{\partial r}|_{\mathrm{r=R}} &= h\left(T(R,t) - T_f(t)\right) \\ -D \frac{\partial C}{\partial r}|_{\mathrm{r=R}} &= k_m\left(C(R,t) - C_f(t)\right) \end{aligned} \tag{4}$$

For the fixed-property preheating calculation, the moisture diffusivity depends on dry-basis moisture according to the empirical relation below. The full-cycle and shrinkage configurations use separate state-dependent property sets.

$$D(C) = 7 \times 10^{-9} e^{-\frac{0.89}{C}} \tag{5}$$

2.3. Shrinkage Mapping and Constitutive Relations

For the full-cycle fixed-radius calculation, the state-dependent properties follow the Appendix 3 empirical correlations (C in kg/kg and T in K):

$$\begin{aligned} \rho(C) &= 650 + 128C \\ c_p(C) &= 1450 + 2736 \frac{C}{C+1} \\ k(C) &= 0.21 + 0.38 \frac{C}{C+1} \\ D(C,T) &= 2.4 \times 10^{-3} e^{-\frac{0.45}{C}} e^{-\frac{3850}{T}} \end{aligned} \tag{6}$$

In the shrinkage-enabled configuration, the measured radius decreases from 2.00 cm to approximately 1.20 cm. The companion empirical property set for this configuration expresses density, specific heat, conductivity, and moisture diffusivity as functions of local moisture and temperature:

$$\begin{aligned} \rho(C) &= 760 + 90C \\ c_p(C) &= 1850 + 2150 \frac{C}{C+1} \\ k(C) &= 0.12 + 0.2 \frac{C}{C+1} \\ D(C,T) &= 4.2 \times 10^{-4} e^{-\frac{0.30}{C}} e^{-\frac{3850}{T}} \end{aligned} \tag{7}$$

The moving physical radius is mapped to a fixed material coordinate. A material point retains its coordinate during uniform radial contraction:

$$\begin{aligned} \xi &= \frac{r}{R(t)} \\ 0 &\le \xi \le 1 \end{aligned} \tag{8}$$

Under this transformation, the moving-boundary moisture balance becomes a diffusion equation on the fixed interval. The energy balance is transformed analogously while retaining its local heat-capacity term:

$$\frac{\partial C}{\partial t} = \frac{1}{\xi R(t)^2}\partial \frac{\partial}{\partial \xi}\left(\xi D(C,T) \frac{\partial C}{\partial \xi}\right) \tag{9}$$

2.4. Numerical Method and Drying Endpoint

A node-centered conservative finite-volume method is used on the radial domain. Related three-dimensional drying simulations and standard numerical heat-transfer treatments provide methodological context for the control-volume and solver choices [13-15]. Fully implicit time stepping forms tridiagonal systems, solved with the Thomas algorithm; Picard iterations update nonlinear properties until successive fields converge. Grid tests span 40–400 radial nodes, and outputs are sampled at 60-s intervals. For the shrinking domain, the same radial material grid is maintained through the coordinate mapping. The completion time is the first instant when the maximum local moisture content satisfies the specified threshold:

$$\tau = \inf\{t : \max_{0 \le \xi \le 1} C(\xi, t) \le 0.15 \mathrm{kg/kg}\} \tag{10}$$

Because the computed radial moisture profile decreases from the center toward the surface, this whole-field criterion is controlled by the center. The model also compares alternative boundary and property simplifications and tests the sensitivity of drying time to convective coefficients.

3. Results and Discussion

3.1. Input Histories and Preheating Response

Figure 1 summarizes the measured chamber temperature and moisture histories and the interpolated material-radius trajectory. Chamber conditions approach their constant-drying values during the first four hours, while radius contraction is most rapid during the first six hours and then slows toward approximately 1.20 cm.

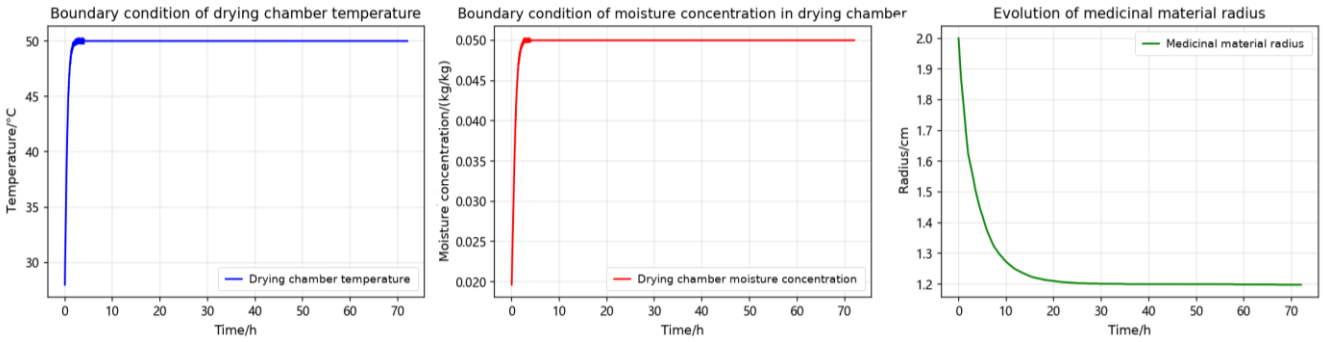

Figure 1. Measured chamber conditions and interpolated material-radius history.

During the initial 30 min, the surface warms faster than the center: at 1,800 s, center and surface temperatures are 33.58 °C and 36.79 °C. Moisture responds on a slower timescale; surface content falls from 2.55 to 1.452 kg/kg while the center remains near 2.55 kg/kg. Figure 2 shows the subsequent radial profiles: by 3 h, the center and surface are at 49.85 °C and 49.97 °C, whereas moisture remains at 1.7651 and 1.0084 kg/kg, respectively. These results distinguish rapid thermal equilibration from delayed internal moisture transport.

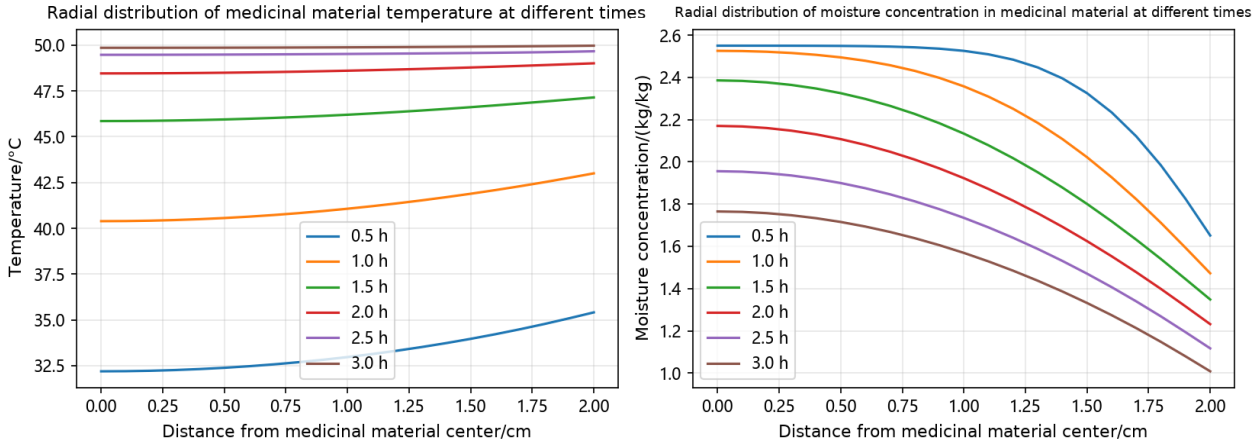

Figure 2. Radial temperature and moisture profiles during preheating.

3.2. Fixed-radius Drying and Numerical Checks

In the variable-property fixed-radius calculation, moisture declines rapidly at first and then enters a prolonged falling-rate period. The center reaches the 0.15 kg/kg threshold at approximately 57.45 h, when surface moisture is 0.0527 kg/kg. Mesh refinement produces drying-time estimates of 57.033 h, 57.350 h, 57.450 h, and 57.483 h for 40, 100, 200, and 400 nodes, respectively. Table 2 summarizes this convergence and the comparisons with simplified formulations.

The 200- and 400-node predictions differ by less than 0.04 h. Omitting external mass-transfer resistance shortens the estimate by about 7.4%; constant diffusivity reduces it by roughly 62%, whereas constant thermal properties change it by only about 0.03%. The lumped model, which removes radial moisture gradients, predicts a substantially shorter duration. Figure 3 illustrates why the endpoint should be based on the wettest position rather than the volume average.

Table 2. Grid convergence and selected model simplification checks.

Test	Configuration	Drying time (h)	48-h profile deviation
Grid	40 nodes	57.0333	2.54×10^{-3}
Grid	100 nodes	57.3500	7.44×10^{-4}
Grid	200 nodes	57.4500	2.22×10^{-4}
Grid	400 nodes	57.4833	Not reported
Boundary	External mass resistance omitted	53.083	—
Property	Constant moisture diffusivity	21.867	—
Property	Constant thermal properties	57.367	—
Geometry	Lumped-parameter model	11.177	No radial field

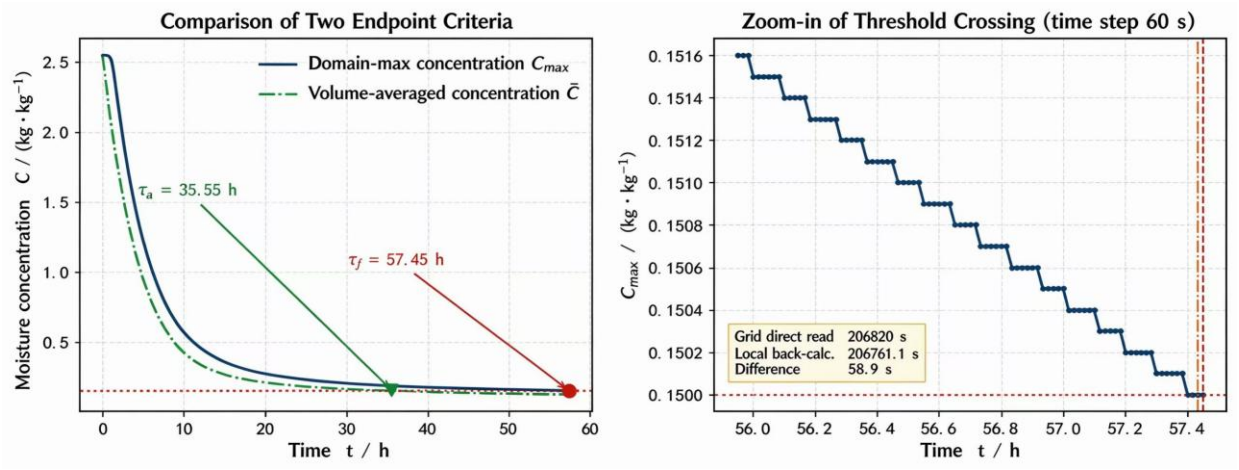

Figure 3. Center and volume-average moisture histories near the drying threshold.

3.3. Shrinkage-enabled Drying

The measured radius falls from 2.00 cm to 1.374 cm during the first 6 h, reaches approximately 1.204 cm by 24 h, and stabilizes near 1.20 cm after about 36 h. The shrinkage-enabled calculation reaches the center-moisture threshold at 51.10 h, with center and surface values of 0.1500 and 0.0526 kg/kg. Figure 4 presents the radial profiles and spatial evolution of moisture in the moving material.

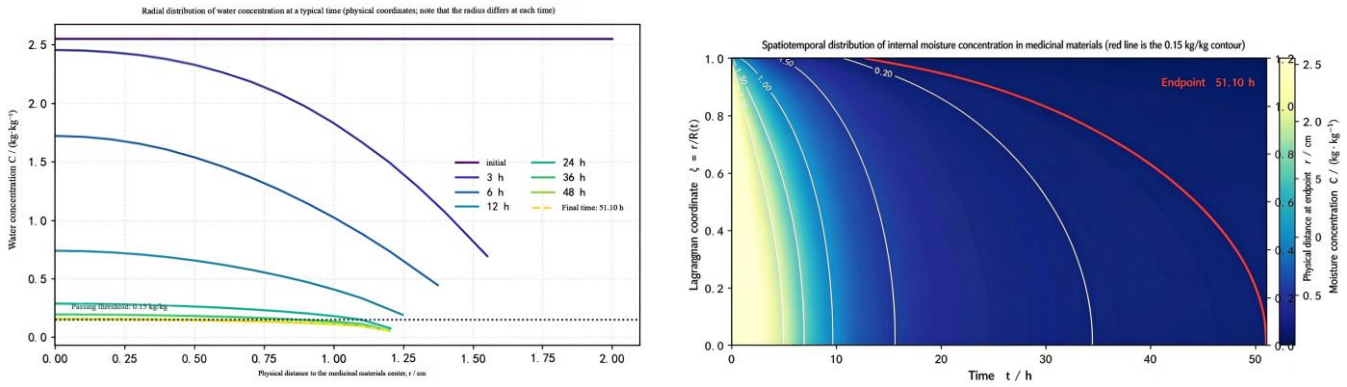

Figure 4. Radial moisture profiles and spatiotemporal moisture evolution in the shrinking domain.

The volume-average moisture reaches 0.15 kg/kg at 34.38 h, 16.72 h before the center reaches the same threshold. This early crossing would not satisfy the whole-field drying criterion. Table 3 compares the two modeled configurations. The fixed-radius case uses the empirical property set associated with that configuration, whereas the moving-radius case uses the separate correlation set specified for shrinkage. The reported time difference is therefore a contrast between the complete configurations, not an isolated estimate of geometry alone.

Table 3. Predicted endpoint values for the two modeled configurations.

Configuration	Property set	Time (h)	Center / surface moisture (kg/kg)	Radius at endpoint
Fixed radius	Appendix 3	57.45	0.1500 / 0.0527	2.00 cm
Measured shrinkage	Appendix 4	51.10	0.1500 / 0.0526	1.20 cm

Figure 5 compares the center-moisture trajectories. The curves cross during the drying process, and the shrinkage-enabled configuration reaches the specified endpoint about 6.35 h earlier. This net contrast is consistent with the shorter late-stage diffusion path, while the distinct empirical property correlations remain part of the comparison.

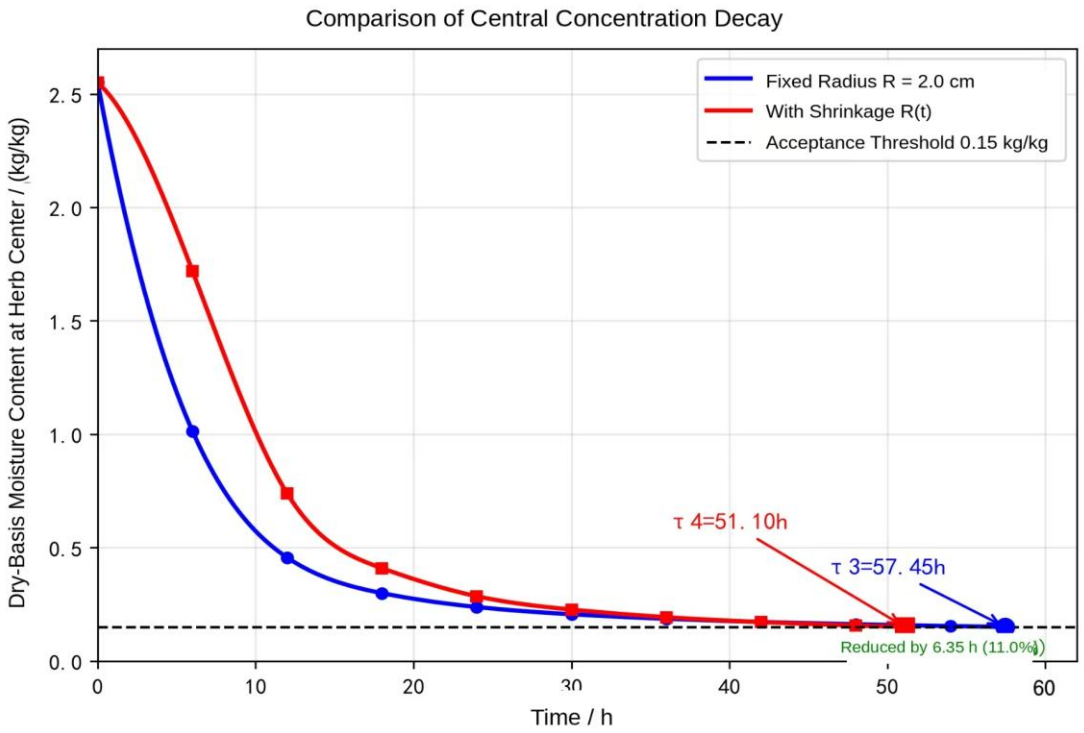

Figure 5. Center-moisture trajectories for the fixed-radius and shrinkage-enabled configurations.

3.4. Sensitivity and Interpretation

Perturbing the heat-transfer coefficient by ±20% changes drying time by no more than 0.03%; a ±20% change in the mass-transfer coefficient changes it by approximately −1.83% to +2.96%. The reported sensitivity therefore indicates that internal moisture diffusion controls most of the drying duration, particularly after the surface approaches its equilibrium moisture level. Related hot-air drying work on Atractylodes macrocephala likewise examines drying kinetics and volatile-component changes [16].

4. Conclusion

A one-dimensional axisymmetric model was formulated to describe heat conduction, moisture diffusion, and measured radial shrinkage during hot-air drying of cylindrical Chinese medicinal material. The conservative finite-volume method, fully implicit stepping, and Picard iteration produced stable results across grid-refinement tests. Under the fixed-radius configuration, the center reaches 0.15 kg/kg after about 57.45 h; the shrinkage-enabled configuration reaches the same local threshold after 51.10 h. The volume-average criterion crosses the threshold substantially earlier and therefore does not ensure that the wettest region is dry. The two reported configurations also use different empirical property correlations, so their time difference represents a combined model contrast. The results support full-field endpoint monitoring and explicit treatment of geometry and property assumptions when estimating drying duration.

Limitations include 1D radial transport, uniform shrinkage, fixed chamber conditions after 4 h, and one material. Future experiments should validate profiles and endpoints for other materials and sizes.

References

[1] Khan, M. I. H., Batuwatta-Gamage, C. P., Karim, M. A., et al. (2022). Fundamental understanding of heat and mass transfer processes for physics-informed machine learning-based drying modelling. Energies, 15(24), 9347.

[2] Gómez-Pérez, L. S., Vega-Gálvez, A., & Moraga, N. O. (2022). Numerical modeling of conjugate heat and mass transfer with water vaporization in solid materials inside a convective hot air tunnel. International Communications in Heat and Mass Transfer, 135, 106144.

[3] Pei, Y., Li, Z., Song, C., et al. (2022). Analysis and modelling of temperature and moisture gradient for ginger slices in hot air drying. Journal of Food Engineering, 323, 111009.

[4] Zhao, H., Dai, J., & Wu, K. (2022). Simulation of coupled heat-mass transfer in sea cucumbers with heat pump drying. Applied Sciences, 12(11), 5508.

[5] Feng, Z., Zheng, X., Ying, Z., et al. (2023). Drying of Chinese medicine residues by hot air for potential utilization as renewable fuels: drying behaviors, effective moisture diffusivity, and pollutant emissions. Biomass Conversion and Biorefinery, 13, 14993–15010.

[6] Tuly, S. S., Joarder, M. U. H., Welsh, Z. G., & Karim, A. (2023). Mathematical modelling of heat and mass transfer during jackfruit drying considering shrinkage. Energies, 16(11), 4461.

[7] Żbik, K., Górska-Horczyczak, E., Onopiuk, A., et al. (2023). Vacuum and convection drying effects on volatile compounds profile and physicochemical properties of selected herbs from Lamiaceae family. European Food Research and Technology, 249, 2569–2581.

[8] Cao, S., Yang, C., Zang, Y., et al. (2023). Simulated and verification of mass and heat transfer coupled model of jujube slices dried by hot air combined with radio frequency heat treatment at different drying stages. Foods, 12(16), 3025.

[9] Zhang, H., Wang, L., Jiang, W., et al. (2025). Numerical simulation and sensitivity analysis of hot air drying for irregular flake materials based on fully coupled of multi-physics fields. Applied Thermal Engineering, 273, 126449.

[10] Teleken, J. T., Amorim, S. M., Rodrigues, S. S., et al. (2025). Heat and mass transfer in shrimp hot-air drying: experimental evaluation and numerical simulation. Foods, 14(3), 428.

[11] Wan, Q., Gao, H., Qi, Y. R., et al. (2023). Research progress and development trends in drying technology and mechanisms of Chinese medicinal extracts. Chinese Traditional and Herbal Drugs, 54(23), 7884–7894.

[12] Xie, H., Qi, Y. R., Wan, N., et al. (2022). Shrinkage mechanisms, influencing factors, and control strategies during drying of Chinese medicinal materials. Chinese Traditional and Herbal Drugs, 53(9), 2872–2881.

[13] Zhang, S. W., Chen, S., Li, X., et al. (2016). Numerical simulation of vacuum drying of maize kernels based on a three-dimensional solid model. Journal of Vacuum Science and Technology, 36(1), 51–56.

[14] Tao, W. Q. (2001). Numerical heat transfer (2nd ed.). Xi'an Jiaotong University Press.

[15] Patankar, S. V. (1984). Numerical heat transfer and fluid flow (Z. Zhang, Trans.). Science Press.

[16] Guo, H. L., Xu, M. T., Wu, Z. F., et al. (2022). Hot-air drying kinetics and volatile-component changes in Atractylodes macrocephala. China Journal of Chinese Materia Medica, 47(4), 922–930.